



Universiteit
Leiden
The Netherlands

Advancing diffusion MRI: improving image quality and getting rid of the fat

Dong, Y.

Citation

Dong, Y. (2024, September 17). *Advancing diffusion MRI: improving image quality and getting rid of the fat*. Retrieved from <https://hdl.handle.net/1887/4092698>

Version: Publisher's Version

License: [Licence agreement concerning inclusion of doctoral thesis in the Institutional Repository of the University of Leiden](#)

Downloaded from: <https://hdl.handle.net/1887/4092698>

Note: To cite this publication please use the final published version (if applicable).

Chapter 6

Structured low-rank reconstruction for navigator-free water/fat separated multi-shot diffusion-weighted EPI

Yiming Dong, Kirsten Koolstra, Ziyu Li, Malte Riedel, Matthias J.P. van Osch, Peter Börnert

Magnetic Resonance in Medicine, 2023;1-16.

Abstract

Purpose: Multi-shot diffusion-weighted EPI allows an increase in image resolution and reduced geometric distortions and can be combined with chemical-shift encoding (Dixon) to separate water/fat signals. However, such approaches suffer from physiological motion-induced shot-to-shot phase variations. In this work, a structured low-rank-based navigator-free algorithm is proposed to address the challenge of simultaneously separating water/fat signals and correcting for physiological motion-induced shot-to-shot phase variations in multi-shot EPI-based diffusion-weighted MRI.

Methods: We propose an iterative, model-based reconstruction pipeline that applies structured low-rank regularization to estimate and eliminate the shot-to-shot phase variations in a data-driven way, while separating water/fat images. The algorithm is tested in different anatomies including head-neck, knee, brain and prostate. The performance is validated in simulations and in-vivo experiments in comparison to existing approaches.

Results: In-vivo experiments and simulations demonstrated the effectiveness of the proposed algorithm compared to extra-navigated and an alternative self-navigation approach. The proposed algorithm demonstrates the capability to reconstruct in the multi-shot/Dixon hybrid space domain under-sampled datasets, using the same number of acquired EPI shots compared to conventional fat-suppression techniques but eliminating fat signals through chemical-shift encoding. In addition, partial Fourier reconstruction can also be achieved by using the concept of virtual conjugate coils in conjunction with the proposed algorithm.

Conclusion: The proposed algorithm effectively eliminates the shot-to-shot phase variations and separates water/fat images, making it a promising solution for future DWI on different anatomies.

6.1 Introduction

Diffusion-weighted imaging (DWI) is a widely used MRI technique that probes tissue microstructure^{7,20}. However, the presence of fat can often be a confounding factor, especially in EPI-based DWI due to the chemical-shift effect^{14,41,77}, and particularly in areas outside the brain, where conventional fat-saturation techniques may be prone to failure^{41,74,76,115}. In addition, the multi-peak nature^{54,116} of the fat spectrum makes it often difficult to fully eliminate all present fat signals under diffusion contrast^{14,41,78,115}. To address these challenges, previous studies proposed to combine DWI with chemical-shift encoding (Dixon), to allow the separation of water and fat signals^{14,41,77,79,115,117}.

In recent years, multi-shot EPI (ms-EPI) has gained popularity in DWI due to its ability to increase spatial resolution and to reduce geometric distortions^{39,67,68,118}. However, multi-shot EPI suffers from physiological motion-induced shot-to-shot phase variations which require corrections using extra navigation, leading to increased scan times^{63,67,68}. Additionally, navigation-free methods^{47–52,119,120} have also been proposed to address the phase variations. Specifically, one series of developed approaches aimed to explicitly estimate the phase map for each shot^{47,48,71}. More recently, techniques inspired by parallel imaging have used structured low-rank constraints^{121–123} to reconstruct the ms-EPI data without explicit phase calculation in either k-space^{51,52,119,120} or image-space^{49,50}.

Additionally, several approaches have been proposed to combine Dixon and multi-shot EPI to obtain fat-free, high spatial resolution DWI^{41,79,115}. However, addressing shot-specific phase issues with extra-navigation can be particularly challenging as the presence of displaced fat signals, overlapping water tissues, can cause phase ambiguities in the reconstruction process^{41,77,115}. Improved approaches, like the Model-based Self-Navigated water/fat Decomposition (MSND)¹¹⁵, allow the self-navigation of the shot-specific phase variations while performing water/fat separation, but it requires an explicit, non-linear shot-to-shot phase estimation which requires appropriate initialization.

In this study, we propose a novel iterative model-based reconstruction approach to combine Dixon imaging and multi-shot DWI, using structured low-rank constraints applied to the water and fat channels to leverage the redundancy across both the chemical shift encoding- and the multi-shot / segmentation dimension. The performance of the new method is compared to the 2D-navigated reconstruction⁴¹ and the navigator-free MSND¹¹⁵ algorithm on

various anatomies and simulations. A disadvantage of using additional Dixon is that it requires multiple echo-shifted scans to fully encode and separate water/fat signals. To address this issue, we investigate the performance of our method regarding under-sampling in the Dixon/multi-shot dimensions. While achieving comparable image quality to conventional fat-saturated multi-shot DW EPI, our method improves scan efficiency due to the elimination of the fat saturation pulse. Finally, we enabled partial-Fourier (pF) sampling in combination with water/fat separation using the virtual conjugate shot (VCS) concept^{52,124}.

6.2 Theory

6.2.1 Water/fat separation for ms-EPI based DWI by chemical-shift encoding (Dixon)

In the Dixon-DW-ms-EPI sequence, the acquisition is repeated N times (typically $N = 3$) at varying ΔTE_n to facilitate additional encoding of water and fat signals. The ΔTE_n is the chemical shift encoding spacing between the EPI readout window's center and the actual spin-echo. The resulting complex ms-EPI signal $b_{n,l,j}(t)$ can be expressed as follows¹¹⁵:

$$\begin{aligned}
 & b_{n,l,j}(t) \\
 &= \int \left[s_j(r) \rho_w(r) + \sum_{m=1}^M \alpha_m s_j(r) \rho_f(r) e^{-i2\pi\psi_{f,m}(\Delta TE_n + t)} \right] e^{-i2\pi B_0(r)\Delta TE_n} e^{-i\varphi_{n,l}(r)} e^{-ik_t \cdot r} dr,
 \end{aligned} \tag{1}$$

where k_t is the k-space sample at time t , with shot or interleave index l , coil j , sampled for the n -th Dixon point. $\rho_w(r)$ and $\rho_f(r)$ represent the complex-valued DW water/fat components at spatial location r , whereas coil sensitivities are indicated by $s_j(r)$. For an M -peak fat model, the relative amplitude and fat off-resonance for each peak m are indicated by α_m and $\psi_{f,m}$, respectively. $B_0(r)$ denotes the B_0 inhomogeneity (in Hz), and $\varphi_{n,l}(r)$ represents the physiological motion-induced shot-to-shot phase variation for each interleave l and Dixon point n . The term in the square brackets models the chemical shift effect of fat relative to the water that is assumed to be on resonance. Furthermore, it is assumed that B_0 -induced dephasing occurring during the readout process can be ignored by approximating $e^{-i2\pi\psi_B(r)(t+\Delta TE_n)} \approx e^{-i2\pi\psi_B(r)\Delta TE_n}$.

Assuming one data set is acquired with a J element coil, N Dixon points, and L shots, to solve for Eq.1, the forward model of the Dixon-based water/fat DW-ms-EPI problem can be written as¹¹⁵:

$$A_0 x = K \begin{bmatrix} I & I \end{bmatrix} \begin{bmatrix} FS\Psi_B P & 0 \\ 0 & \Psi_f FS\Psi_B P \end{bmatrix} \begin{bmatrix} x_w \\ x_f \end{bmatrix}, \quad (2)$$

Where matrix/operator K indicates the shot-specific k-space trajectory which is applied for masking out unacquired k-space lines of each shot/Dixon point, I is the identity matrix for combining water/fat channels, F is the Fourier transform, Ψ_f adds fat off-resonance, according to the chosen multi-peak fat spectrum model^{41,53,54}, S adds the coil sensitivity weighting, Ψ_B adds the B_0 inhomogeneity-induced phase, P adds the physiological motion induced phase of each shot/Dixon point and $x = [x_w, x_f]^T$ represents the joint water/fat magnitudes to be reconstructed. In Ψ_B and Ψ_f , the multiple ΔTE_n are included in the phase terms $e^{-i2\pi B_0(r)\Delta TE_n}$ and $e^{-i2\pi\psi_{f,m}(\Delta TE_n + t)}$ for Dixon as shown in Eq.1. More details about the construction of all operators can be found in the Supporting Information Table S.1.1.

6.2.2 Structured low-rank constraints for Dixon-DW-ms-EPI DWI

In MUSSELS^{51,52}, which was proposed to reconstruct fat suppressed ms-EPI DW images without extra navigation, the low-rank constraint leverages redundancy across shots by assuming that the underlying magnitude components are equal, whereas the shot-to-shot phase can be different. Under the assumption that the physiological motion-induced phase varies smoothly in image space, one can construct such a block-Hankel matrix, from the stacked and lifted k-space shot data with the annihilating filter in k-space. The resulting block-Hankel matrix has a non-zero null space and is thus low-rank as described in ref.⁵¹. Therefore, the low-rank structure can be enforced to guide the reconstruction by minimizing its nuclear norm, sharing magnitude information between the different shots while maintaining shot-specific phase informatio^{51,52,119}. Such low-rank regularization can also be applied to Dixon-DW-ms-EPI data, with the aim to jointly reconstruct water and fat magnitudes and to correct the fat chemical-shift-induced displacements along with shot-to-shot phase estimation.

First, Eq.2 can be rewritten into a form in which the series of shot-individual water/fat complex images are estimated jointly:

$$A\hat{x} = K \begin{bmatrix} I & I \end{bmatrix} \begin{bmatrix} FS\Psi_B & 0 \\ 0 & \Psi_f FS\Psi_B \end{bmatrix} \begin{bmatrix} \hat{x}_w \\ \hat{x}_f \end{bmatrix}, \quad (3)$$

where $\hat{x} = [\hat{x}_w, \hat{x}_f]^T$ are the complex water/fat shot images (including shot-to-shot phase variations as described by P in Eq.2), having L shots and N Dixon points, forming a two-dimensional encoding space (multi-shot/Dixon). Like MUSSELS, it is assumed that the water magnitude and fat magnitude images are constant within a dataset but that the phase varies for different shots/Dixon points. The cost function of the Dixon-DW-ms-EPI reconstruction with structured low-rank constraints can subsequently be written as:

$$\{\bar{x}_w, \bar{x}_f\} = \underset{\hat{x}_w, \hat{x}_f \in \mathbb{C}^{Q \times N \times L}}{\operatorname{argmin}} \quad \|A\hat{x} - d\|_2^2 + \lambda_1 \|H(F\hat{x}_w)\|_* + \lambda_2 \|H(F\hat{x}_f)\|_*, \quad (4)$$

where Q is the number of voxels, d is the k-space raw data, and λ_1/λ_2 denote regularization factors for water/fat channels. $\|H(F\hat{x}_{w/f})\|_*$ are the block-Hankel regularization terms for water and fat images, respectively. The minimization of the nuclear norm is reformulated as an iterative reweighted least-square (IRLS)^{52,125} approach for acceleration. The implementation details can be found in Supporting Information Table S.1.2. It should be noted that water/fat signals experience the same water-fat-combined phase offset¹¹⁵, after correcting for the spatial displacement of fat. These water/fat combined, but shot-specific phases, calculated as $[\varphi_{1,1}, \dots, \varphi_{N,1}, \dots, \varphi_{1,L}, \dots, \varphi_{N,L}]^T = \angle(\hat{x}_w + \hat{x}_f)$, are updated individually for each shot. To enforce the magnitude similarity^{47,49-52,115,119}, the water/fat magnitude images for different shots are replaced by their averages (i.e., $\tilde{x}_{w/f} = \sum_{n=1}^N \sum_{l=1}^L |x_{w/f,n,l}| / (N \times L)$, where $\tilde{x}_{w/f}$ are averaged magnitudes of the water/fat images) after each iteration to help preventing the optimization from getting stuck in a local minimum and to guarantee convergence. This additional step, which is different from MUSSELS, is newly proposed in this work. The updated complex water/fat shot images can therefore be formulated as:

$$\hat{x}_{updated} = [\tilde{x}_w e^{i\varphi_{1,1}}, \dots, \tilde{x}_w e^{i\varphi_{N,1}}, \dots, \tilde{x}_w e^{i\varphi_{1,L}}, \dots, \tilde{x}_w e^{i\varphi_{N,L}}, \tilde{x}_f e^{i\varphi_{1,1}}, \dots, \tilde{x}_f e^{i\varphi_{N,1}}, \dots, \tilde{x}_f e^{i\varphi_{1,L}}, \dots, \tilde{x}_f e^{i\varphi_{N,L}}]^T. \quad (5)$$

The whole pipeline is described in figure 1. Assuming similar B_0 conditions for $b=0$ s/mm² and $b>0$ s/mm² measurements, a B_0 map can be estimated based on the $b=0$ s/mm² data,

serving as a prior for the diffusion case¹¹⁵. Each $b > 0$ s/mm² dataset is reconstructed individually in the current pipeline.

6.2.3 Enabling partial-Fourier acquisition by using virtual conjugate shots (VCS) for water/fat separation

To achieve shorter TE, Partial-Fourier is an option, but it represents a challenging problem in both Dixon and DW ms-EPI reconstructions, since it requires the signal under estimation to be real-valued⁹¹. In this case, the conjugate symmetry property^{50,52,124} can be used to reconstruct the partial-Fourier k-space data by adding the VCS when constructing the water/fat Hankel matrices as:

$$H(F\hat{x}_{w/f}) = [H_{w/f,1,1}, \dots, H_{w/f,n,1}, \dots, H_{w/f,n,l}, H_{w/f,1,1}^\dagger, \dots, H_{w/f,n,1}^\dagger, \dots, H_{w/f,n,l}^\dagger], \quad (6)$$

where $H_{w/f,n,l} = H(Fx_{w/f,n,l})$ indicates the Hankel matrix of the n -th Dixon point and l -th shot ($n = 1, 2, \dots, N; l = 1, 2, \dots, L$) and † indicates the conjugate flipping of the k-space data along both directions^{50,52,124}. This operation enables the reconstruction of partial-Fourier data to fill the missing k-space lines while performing water/fat separation.

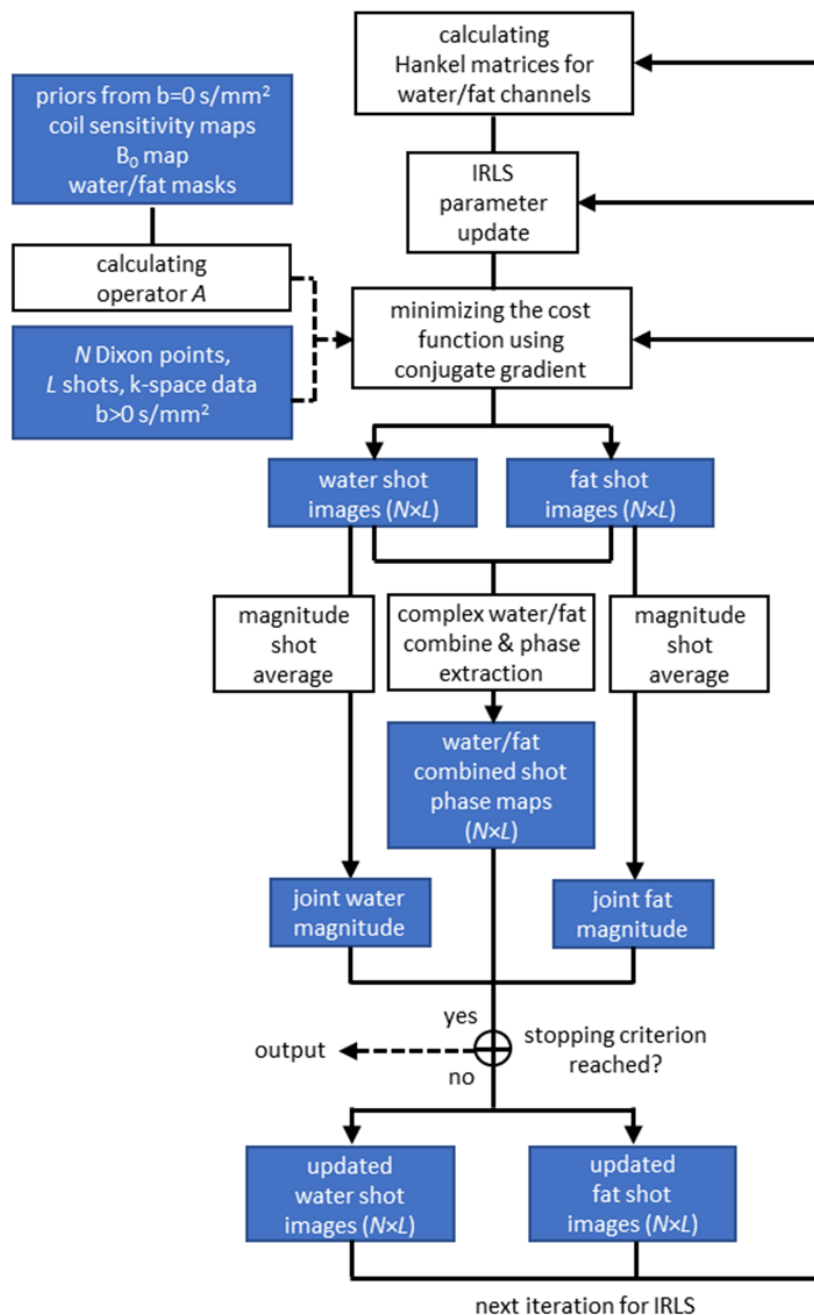


Figure 1. Reconstruction pipeline of the proposed algorithm. The matrix A is first computed using information from a non-diffusion scan. In each iteration, two series of water/fat shot images (consisting of N Dixon points and L shots) are calculated using Hankel matrices as regularization terms. The water/fat combined phase maps are then computed by combining the water/fat shot complex images and extracting their phases. Additionally, the water/fat magnitudes of all shots are averaged to generate one joint water magnitude and one joint fat magnitude, to accelerate the convergence. The updated water/fat complex shot images are then generated using the combined phase maps and the joint water/fat amplitude images through Eq.5. Then, in the next iteration the two SVD are performed for water/fat channels separately, with the iterative reweighted least-square (IRLS) parameters calculated and updated. The pseudo-code can be found in Supporting information Table.S.1.2.

6.3 Methods

6.3.4 Simulations

A simulation was performed to evaluate the performance of 2D-navigated-, MSND-, and the proposed structured low-rank based approaches, under different SNR conditions. Shepp-Logan water-fat k-space data were simulated, according to Eq.2, assuming an 8-element cylindrical head coil with simulated coil-sensitivity maps (CSM). Dixon-ms-EPI datasets with 4-shots and 3 Dixon points ($\Delta TE=0.2/1.0/1.8\text{ms}$) were simulated to match the in-vivo scans of this work. The physiological motion induced shot-to-shot phase variations were simulated based on 12 measured 2D-navigators of a fat-suppressed brain scan, using interpolation/extrapolation to cover the whole phantom. SNR was varied by adding complex Gaussian noise to the simulated water/fat images for each coil and every shot/Dixon point. The SNR range of each coil image was chosen between 2 to 20, with SNR defined as the ratio of averaged signal magnitude within the signal-bearing parts of the phantom to synthetic noise standard deviation. 2D-navigators were simulated for each shot via fully sampled ss-EPI data with the fat signal displaced along phase-encoding direction, matching the bandwidth of the 4-shot EPI data for simplification. Please note, this is not the case for the real measurements since under-sampling was often used to match the bandwidth between the low-resolution 2D-navigator with the ms-EPI data. The signal decay due to T2 (50ms) was considered and simulated using TEs between image/navigator of 70ms/120ms. The simulation matrix size was set to 120×120 , with bandwidth in phase-encoding direction of 20 Hz/pixel. A multi-peak fat model was used to simulate the chemical-shift effect for fat⁴¹. The geometric distortion was not considered in the simulation.

6.3.5 In-vivo experiments

Chemical-shift encoded spin-echo diffusion-weighted 4-shot-EPI (Dixon-DW-ms-EPI) was employed in a series of experiments to investigate various regions, including the brain, head-neck, knee, and prostate, in 9 healthy volunteers using a 3T Philips scanner (Best, The Netherlands). Informed consent was obtained from each participant and approved by the local ethics committee. Different coils were used for each region: a 15-channel head-neck coil for the brain and head-neck regions, a 16-channel knee coil for the knee, and a 16-channel anterior coil and a 12-channel posterior coil for the prostate. Out of the 9 volunteers, 4 were scanned in brain, 2 in head-neck, 1 in leg, and the remaining 2 were scanned in the prostate

region. Informed consent was obtained from all volunteers prior to the experiments. To enable 3-point water-fat chemical-shift encoding, the EPI readout window was shifted asymmetrically by a given ΔTE with respect to the actual spin echo^{41,115}. All scans were acquired with a TR of 5s and no parallel imaging acceleration was used. One subject's brain was additionally scanned with a 4-point Dixon sequence to obtain an equal number of Dixon points and EPI shots (4-point Dixon vs. 4-shot EPI). In this volunteer and in another one, scanned in prostate, additionally conventional SPIR⁴³ fat suppressed DW 4-shot EPI were acquired, for comparison. All other important scan parameters are listed in Table 1. For all relatively high-resolution scans, an extra 2D navigator was acquired for each diffusion shot to allow comparison of the proposed algorithm with navigator-based reconstructions.

Table 1. Sequence parameters

anatomy	resolution (mm ³)	matrix size	TE (ms)	pF ^a factor	ΔTE (ms)	b-value (s/mm ²)	Fat sat.	shot readout duration time (ms)	number of phase encoding lines per shot
leg	1.4 x 1.5 x 4	152 x 148	69	-	0.2 / 1.0 / 1.8	0,300,600	-	27.6	37
head-neck	1.4 x 1.5 x 4	152 x 148	69	-	0.2 / 1.0 / 1.8	0,300,600	-	27.6	37
brain	1.0 x 1.0 x 4	232 x 228	103	-	0.2 / 1.0 / 1.8	0,1000	-	58.7	57
	1.0 x 1.0 x 4	232 x 228	103	-	0.2 / 0.7 / 1.3 / 1.8	0,1000	-	58.7	57
	1.0 x 1.0 x 4	232 x 228	103	-	0.0	0,1000	SPIR	58.7	57
prostate	1.0 x 1.0 x 4	232 x 228	74	0.632	0.2 / 1.0 / 1.8	0,500	-	59.0	36
	1.0 x 1.0 x 4	232 x 228	74	0.632	0.0 / 0.0 / 0.0 ^b	0,500	SPIR	59.0	36

^apF factor: partial-Fourier factor along phase encoding direction

^b: no Dixon was applied but instead 3 scan averages (NSA) to match the SNR

6.3.6 Reconstruction

For the simulation, the 2D-navigated data was reconstructed using the model-based water/fat separation in MSND, adding the synthetic phase maps which have the shifted fat signal present, skipping the phase estimation step. The MSND method was implemented based on the original work but with 50 iterations for the outer Gauss-Newton loop and 20 iterations for the inner CG (conjugate gradient) loops. The proposed structured low-rank approach was running with 50 outer IRLS loops and 20 for the inner preconditioned CG using a filter size =

4×4 for the block-Hankel matrices. Following each iteration, both the MSND and the proposed algorithm adopted a triangular filter in k-space on the phase maps. The use of filters to smooth phase maps and minimize noise enhancement from iterative solvers is a common operation described in different studies^{45,47,115,126–128}, particularly in low SNR scenarios. The triangular filter was used after each outer iteration (Gauss-Newton for MSND and IRLS for the proposed algorithm) with a window width of 1/4 the matrix size, which was kept constant for all SNR values to maintain consistent reconstruction scenarios.

For the in-vivo measurements, a B_0 map prior and coil-sensitivity maps can be calculated/calibrated using an image-based water/fat decomposition approach for EPI (IDE)⁴¹ and ESPIRiT⁹² as described in ref.¹¹⁵ based on $b = 0$ s/mm² data. Similar to ref.⁸, two masks (water and fat) can be created by thresholding the $b = 0$ s/mm² water/fat images respectively. Those have a higher SNR than the DW data. The masks were determined empirically by 5%-thresholding the maximum signal intensity observed in the water/fat images, respectively. A binary dilation step was empirically performed (two iterations for fat, one for water), to counteract potential edge artifacts. Please note, these masks are not complementary and will overlap in case of substantial partial volume effects. The CSMs were then masked with these water/fat masks to stabilize the reconstruction, similar to previous works^{60,86,115}. For all reconstructions, a multi-peak fat model⁴¹ was used.

When reconstructing partial-Fourier data for the prostate, direct B_0 estimation can lead to inaccuracies due to partial-Fourier induced blurring effects. To mitigate this problem, the B_0 map was computed on a lower resolution, using the available k-space center data (roughly 1/4 of the original matrix size). The B_0 map estimated by IDE was then interpolated back to the original matrix size.

For the reconstruction of the DW data, using the proposed algorithm, the outer IRLS loops were ran for 16 iterations and 8 iterations for CG, with a filter size of 4×4 for the block-Hankel matrices and $\lambda_1 = \lambda_2 = 0.002$ chosen empirically. After each outer iteration, a triangular filter^{45,47,115,126–128} with a window width equivalent to the matrix size was applied to the combined water/fat phase maps to mildly reduce noise propagation. For comparison, the IDE⁴¹ algorithm was used to reconstruct the data using phase maps extracted from the 2D-navigators⁶³, as an example for the navigated reconstruction. As another reference method, the explicit-phase-estimated MSND reconstructions were performed with all hyperparameters chosen the same as in the original work¹¹⁵.

The retrospectively under-sampled 4-shot/4-Dixon data were generated using different under-sampling schemes to mimic reduction factors $R=2$ and $R=4$. The latter one, used in total 4-shots (each using different ΔTE shifts), was compared with a conventional SPIR-on DW-ms-EPI dataset, which utilized the same number of acquired EPI shots. Similarly, a 4-shot/3-Dixon brain dataset was retrospectively under-sampled to assess the effects of using different under-sampling patterns. In addition, two fully sampled 3-point Dixon DW ms-EPI datasets were used to retrospectively simulate partial-Fourier (pF) data by setting the relevant parts of k-space to zero to mimic a partial-Fourier ratio of 0.6. For virtual conjugate shots (VCS) reconstruction for both in-vivo and simulated data, the regularization factors were changed to $\lambda_1 = \lambda_2 = 0.001$.

Coil compression was performed for all datasets, keeping only 8 virtual coils for reconstruction acceleration. All implementations were done in GPU-supported python 3.8, using GPU/CPU NVIDIA QUADRO RTX 6000/ Intel Xeon Gold 6234. The maximum reconstruction time (16 IRLS iterations) for typical 3-point Dixon /4-shot scans was 16.8 s for a 232×228 matrix and 7.5 s for a 152×148 matrix. Under-sampled ($R=4$) data took 3.7 s and pF with VCS took 48 s (both with a 232×228 matrix size).

6.3.7 Evaluation criteria

In the simulation experiment, quantitative evaluations were conducted by calculating the nRMSE between the reconstructed water image and the groundtruth water image (with synthetic noise added) for each simulation. The nRMSE was calculated by: $nRMSE = \sqrt{\sum_{q=1}^Q (\hat{x}_q - x_q)^2 / Q} / \bar{x}_q$, where \hat{x}_q is the groundtruth water magnitude, x_q the water result, \bar{x}_q the average amplitudes of the groundtruth and Q the number of voxels. In the in-vivo experiments, the nRMSE was calculated in the same manner between the reference image and the evaluated image.

In addition, when comparing Dixon and SPIR data with the same number of signal averages (NSA), the structural similarity index (SSIM)¹²⁹ was calculated to judge image quality. However, measuring the actual SNR is challenging. Therefore, the apparent SNR (aSNR) was calculated as the ratio of the mean signal intensity within a selected ROI divided by the corresponding standard deviation. ROIs were chosen in the frontal brain regions, primarily targeting white matter and assuming minimal intensity variation within each ROI. To prevent

data inconsistencies, caused by rigid motion between two scans, each slice of SPIR data was registered to the Dixon data before subsequent analysis.

6.4 Results

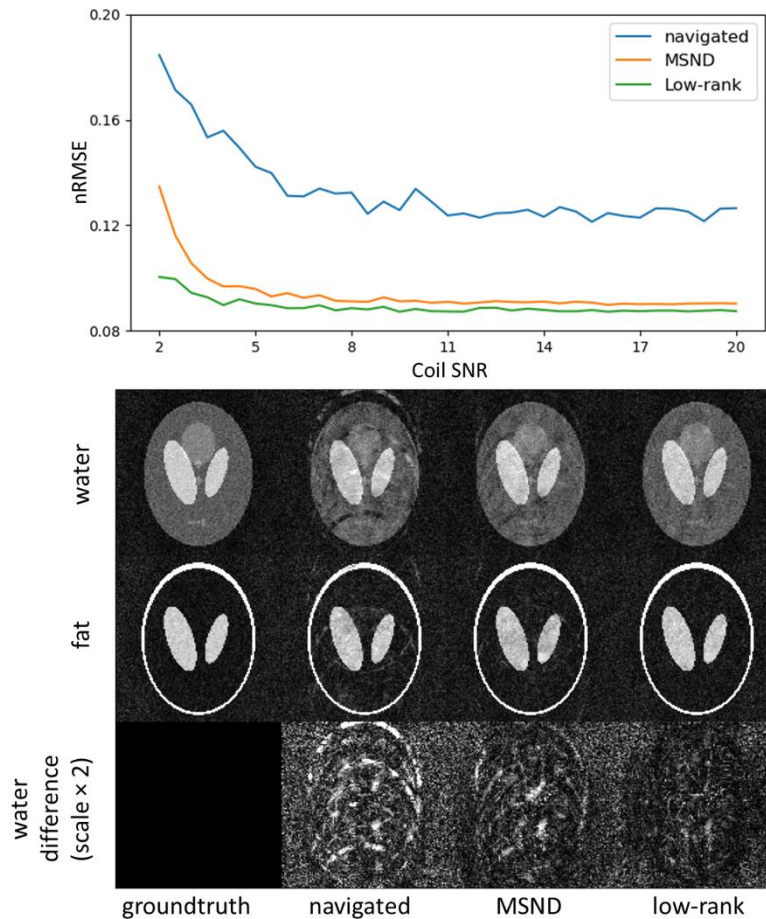


Figure 2. Comparison of three different reconstruction approaches (extra-navigated, MSND, and low-rank) using simulated DWI data. (Top) Normalized root mean squared errors (nRMSE) of the water images for the different approaches given as a function of varying SNR in each individual coil element (coil SNR). The proposed low rank-based reconstruction shows better performance compared to MSND and navigated methods in all cases. The extra navigated approach’s nRMSE is dominated by the phase errors caused by the shifted fat in the navigator signal. (Bottom) Water/fat results for one example case (coil SNR=2), as well as the difference maps to the reference ground truth, demonstrate the better performance of the proposed algorithm showing less artifacts in such low SNR condition.

Figure 2 shows a comparison of three different reconstruction approaches, based on simulated data with varying SNR of each individual coil element, using the nRMSE for error quantification. Water results for one example (coil SNR=2) as well as corresponding difference maps illustrate the better performance of the proposed algorithm. The proposed algorithm outperforms MSND by incorporating a low-rank constraint for complex k-space

estimation. This approach avoids the explicit computation of the Jacobian matrix through an operator formulation of the Gauss-Newton loop in image space, resulting in improved performance, especially in low-SNR cases. Thus, the low-rank constraint provides a more effective solution for joint magnitude and phase reconstruction while avoiding noise enhancement.

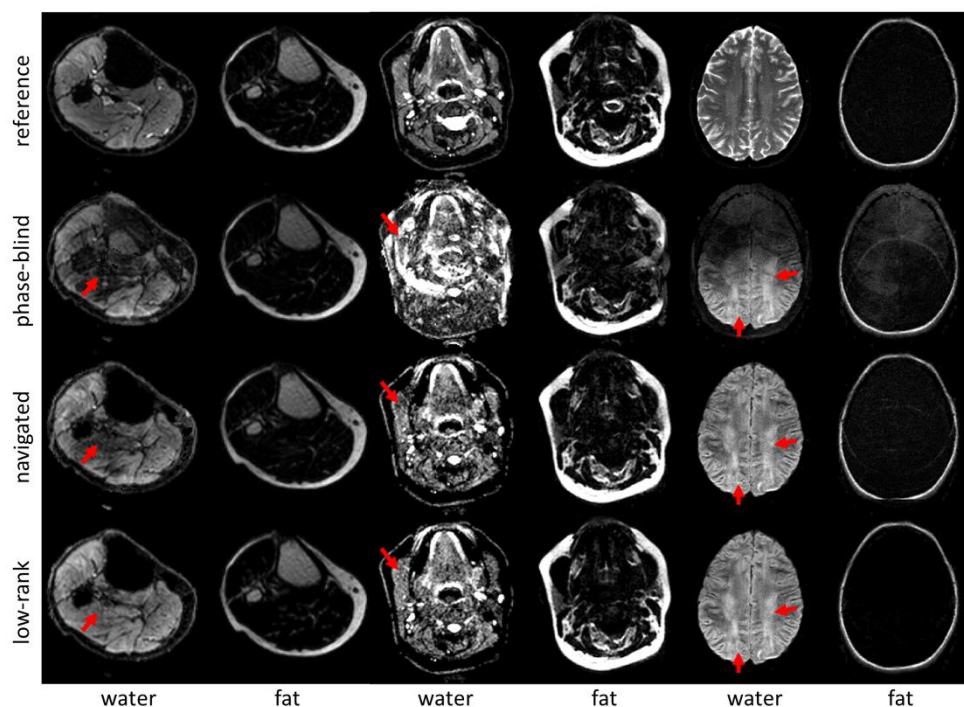


Figure 3. Water/fat resolved DWI results for three various anatomies (knee and neck at $b = 600$ s/mm^2 , and brain at $b = 1000$ s/mm^2) reconstructed with three different reconstruction methods. (Top row) $b = 0$ s/mm^2 images included for anatomical reference. It should be noted that some signal non-stationarities, caused by unsuppressed CSF pulsatility or flow, may result in further aliasing in the reference images. (Second row) water/fat results for a phase-blind SENSE reconstruction (i.e., reconstructing without any shot-specific phase information). (Third row) result obtained using the extra-navigator, and (fourth row) result obtained using the proposed algorithm. The red arrows highlight the artifacts created when using extra-navigators in which the displaced fat signals are present. The proposed method addresses the issue of inaccurate phase information resulting from shifted fat in certain regions and produces better results. For the mid-resolution head-neck scan, the shot duration without/with navigators was 85/117 ms, respectively, illustrating the gain in acquisition efficiency.

Figure 3 shows representative in-vivo results of knee, head-neck, and brain data, reconstructed using measured navigators and the proposed navigator-free approach. In all phase-blind reconstructions, the neglected physiological motion-induced phase variations heavily degrade the water/fat separation quality. In the navigated results, artifacts are clearly visible mainly caused by unsuppressed fat signal present in the extra-navigators¹¹⁵. In contrast, the water/fat separation results from the proposed method achieved the best quality

for all anatomies. Additional slices, showing similar results, can be found in Supporting Information Figure S.1.

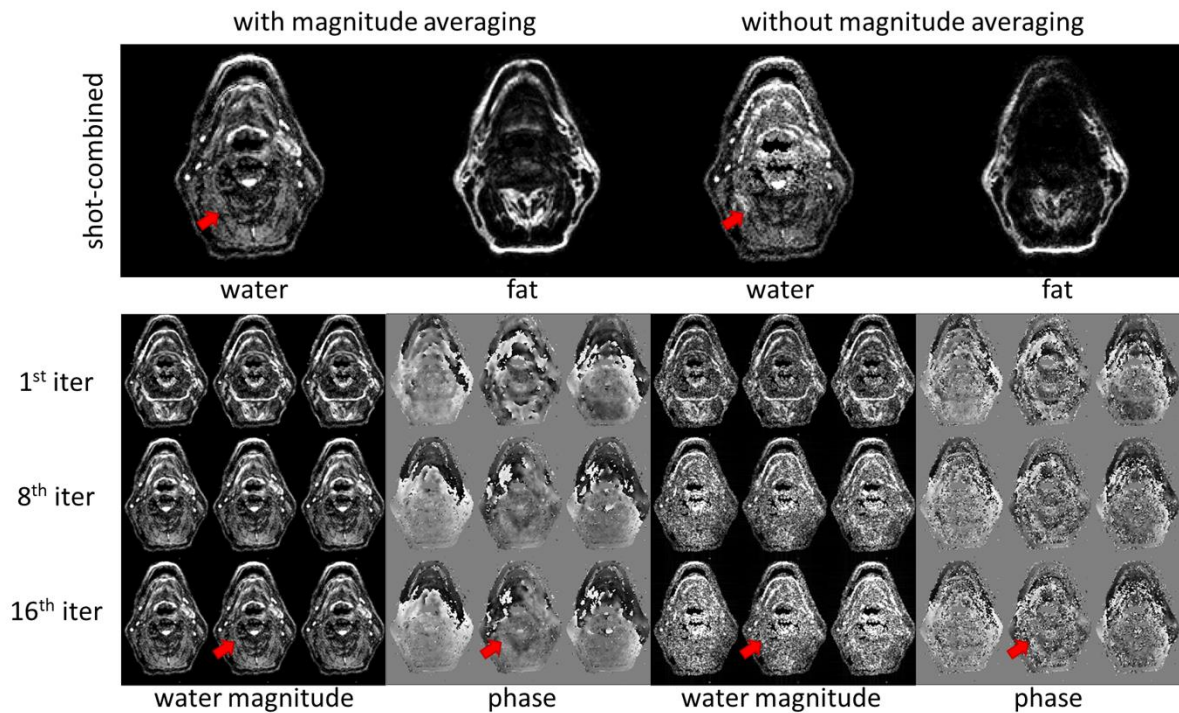


Figure 4. Low-rank reconstructed water/fat-resolved head-neck images with and without magnitude averaging ($b=600 \text{ s/mm}^2$). The final shot-combined water/fat images and the 1st, 8th and 16th outer iteration water images and diffusion-induced shot phase maps (water/fat combined) of three example EPI shots (12 in total) are shown. Applying structured low-rank regularizations without magnitude averaging produced some fat-related artefacts in the shot-combined water channel (marked by red arrows). Probably, the optimization suffered from the low spatial-SNR, causing the phase estimation trapped into some erroneous local minima (red arrows). The implementation of the proposed magnitude averaging step results in a better conditioned optimization problem. This process eliminates such artifacts, giving significantly improved water/fat separated images.

Figure 4 illustrates the convergence behavior of an example head-neck slice using the proposed algorithm, with and without the magnitude averaging step. The observed improvement in the results with magnitude averaging is due to several factors. First, it reduces the number of unknowns in the optimization problem by seeking only two averaged water and fat magnitudes across all images/Dixon points while maintaining different phase maps. This leads to a higher SNR in each estimation iteration, which in turn prevents the algorithm from being compromised by noise and getting trapped in a local minimum. As a result, the problem is better conditioned and it converges in all analyzed cases.

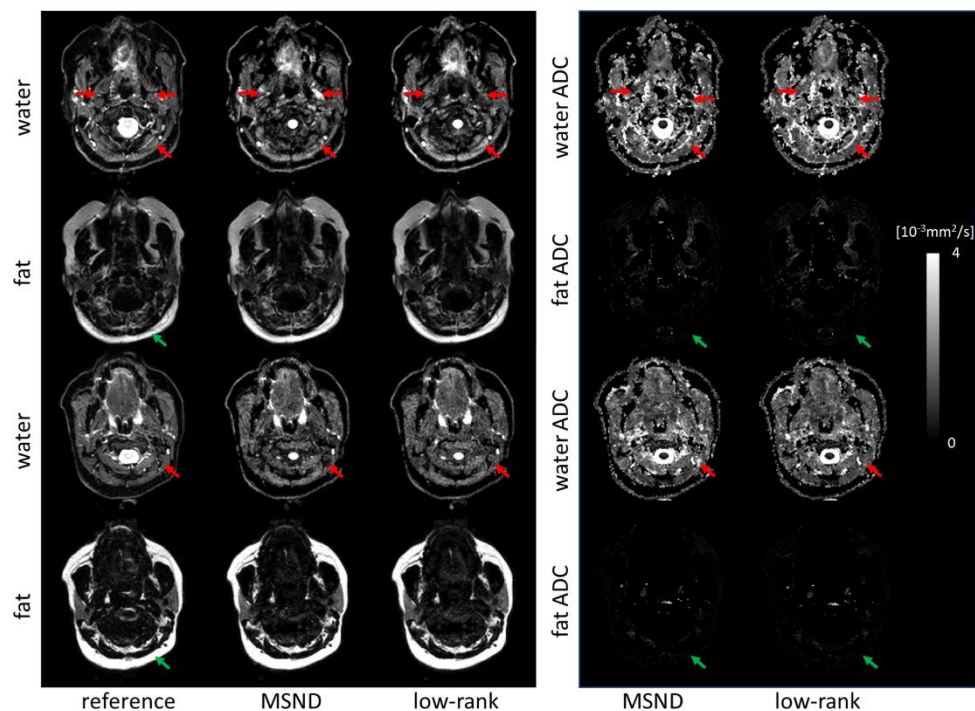


Figure 5. Comparison between MSND and the low-rank regularized approach for DWI ($b = 600$ s/mm²) in the head-neck region of two slices from one subject. The non-diffusion ($b = 0$ s/mm²) water/fat separated data are shown as anatomical reference (first column). In some critical regions, some artifacts and signal cancellation can be observed (red arrows) when using MSND but can be avoided using the low-rank method. These effects can also be seen in the associated ADC maps. The abnormal ADC values in the marked regions (red arrows) in MSND were corrected in the low-rank reconstructions. Due to the low diffusivity of fat signals, the ADC values in fat regions are close to zero (green arrows).

Figure 5 shows in-vivo data in the head-neck region of two subjects comparing MSND and the proposed low-rank-based approach. Although both algorithms rely on the same signal model, the proposed algorithm, that includes low-rank constraints, shows better performance in some challenging regions (red arrows). Furthermore, a comparison of the phase maps acquired by using measured extra-navigators, MSND and the proposed algorithm is shown in Supporting Information Figure S.2.

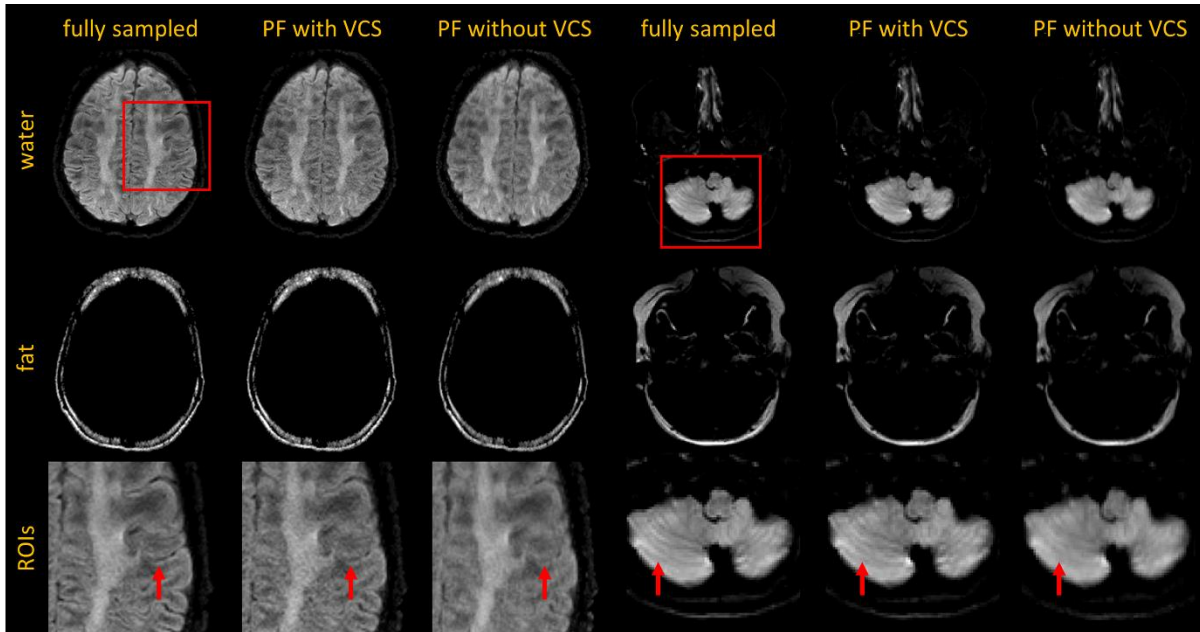


Figure 6. Low-rank partial-Fourier (pF) water/fat-resolved reconstructions of (A) one subject's brain data ($b=1000$ s/mm²) and (B) another subject's cerebellum ($b=600$ s/mm², head-neck scan). Fully sampled DW images are shown for anatomical reference, along with proposed structured low-rank-based solutions with and without (simply zero-padded) VCS, with water at the top, fat in the middle, and water close-ups in the bottom row. The loss of spatial resolution (blur) in the zero padded-reconstructions is obvious in comparison to the fully sampled solution. However, the application of VCS can effectively improve the reconstruction, bringing the image much closer to the quality of the fully sampled case. Furthermore, the slight loss in SNR in the pF data is visible. The red arrows point to the same brain anatomy to ease comparison.

Figure 6 shows retrospectively generated partial-Fourier 4-shot data of one subject's brain and one subject's cerebellum (from a head-neck scan), reconstructed with/without VCS. This is compared to the fully sampled reconstruction. With the help of VCS, the image blurring caused by missing data in partial-Fourier was reduced.

Figure 7(A) compares under-sampled 4-shot brain images with conventional fat-suppressed (SPIR) ms-EPI data (no Dixon dimension), using the nRMSE related to the R=1 case to indicate the SNR loss due to under-sampling. The R=1 and R=2 cases benefited from inherent signal averaging during reconstruction, resulting in higher SNR. The R=4 case improves acquisition efficiency by eliminating fat saturation, resulting in image quality comparable to SPIR data (having the same NSA=1). Figure 7(B) compares the under-sampling in the Dixon-shot encoding space using 3-point Dixon and 4-shot data with different under-sampling patterns. The R=3 case covered the entire k-space despite two shots have the same ΔTE . Two R=4 cases show that covering more lines in k-space results in smaller nRMSE and fewer artefacts (yellow arrows). A comparison between MSND and the

proposed method for under-sampled data ($R=3$) is shown in Supporting Information Figure S.3.

Figure 8 compares four under-sampled Dixon water slices with corresponding SPIR slices at the same $NSA=1$ ($R=4$ for the 4-point Dixon / 4-shot data with full k-space coverage). In the four selected ROIs, the aSNR values are similar, mainly due to the same NSA in both cases. However, a slight decrease in aSNR for the SPIR results can potentially be attributed to the use of extra-measured navigators³⁹. Across the entire FOV, no obvious fine structures are observed in the difference maps, except for some discrepancies at brain edges (e.g., at the bottom left of slices 2 and 3), possibly due to imperfect registration. In addition, the relatively high SSIMs and low nRMSEs between the two techniques indicate comparable image quality when fat suppression is effective.

Figure 9 displays prostate water/fat results from two subjects. One subject was additionally scanned with SPIR (with the same $NSA=3$), where failures in fat suppression can be observed for both the main fat peak (-3.4 ppm relative to water) and the olefinic peak (0.61 ppm relative to water). Although the displaced subcutaneous main-peak fat signals do not cover crucial prostate tissue in this 4-shot EPI experiment, different scan settings could still cause interference (e.g., when the bandwidth is reduced in phase-encoding direction). In contrast, the Dixon method effectively removes most remaining fat signals, providing greater flexibility in choosing scan parameters.

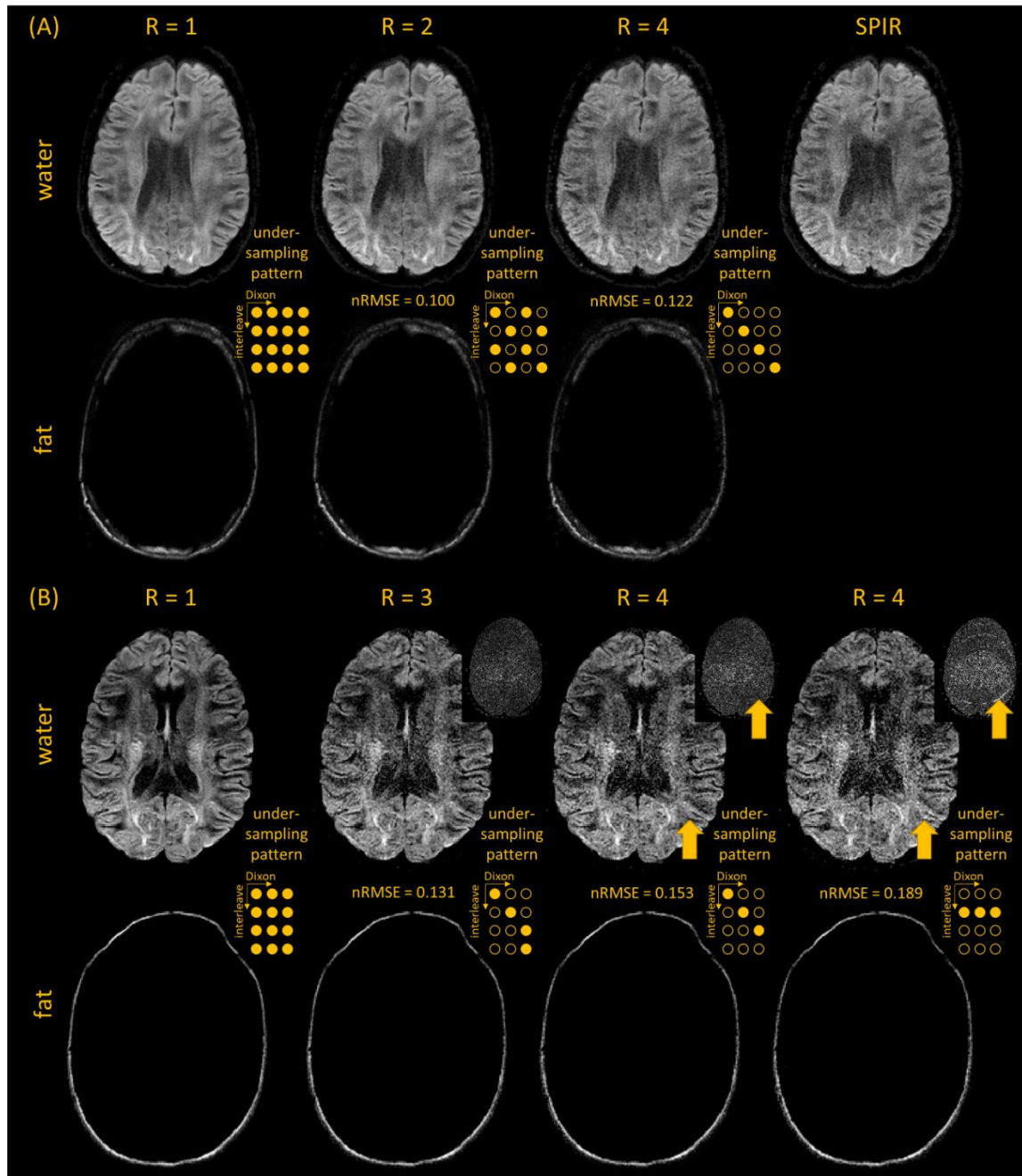


Figure 7. Comparison of undersampled low-rank-reconstructed water/fat results for two representative subjects (DWI, $b=1000$ s/mm²). (A) Illustrates the differences in k-space sampling patterns (reduction factor $R=1, 2, 4$) using 4-point Dixon /4-shot data and compared to fat suppression (SPIR) data. The nRMSEs, relative to $R=1$, indicate a decrease in SNR with increasing R . For $R=4$, the Dixon scan time is comparable to a conventional fat-suppressed DW 4-shot EPI (SPIR), maintaining visible SNR and image quality. Note that the 2D under-sampling pattern used is illustrated by the small matrices to the right of each image, with filled circles indicating data used in the reconstruction and open circles not used. (B) Comparison of different k-space sampling patterns ($R=1, 3, 4, 4$) using 3-Dixon points / 4-shot data, with difference maps (shown top right, upscaled $\times 5$) between each under-sampled case and $R=1$. A $R=3$ example is selected covering the full encoding space. Two different $R=4$ patterns were selected, resulting in different reconstruction problem conditions and artifact removal abilities (yellow arrow). This is reflected in the increase of nRMSE, given relative to the $R=1$, highlighting the overall SNR reduction due to under-sampling.

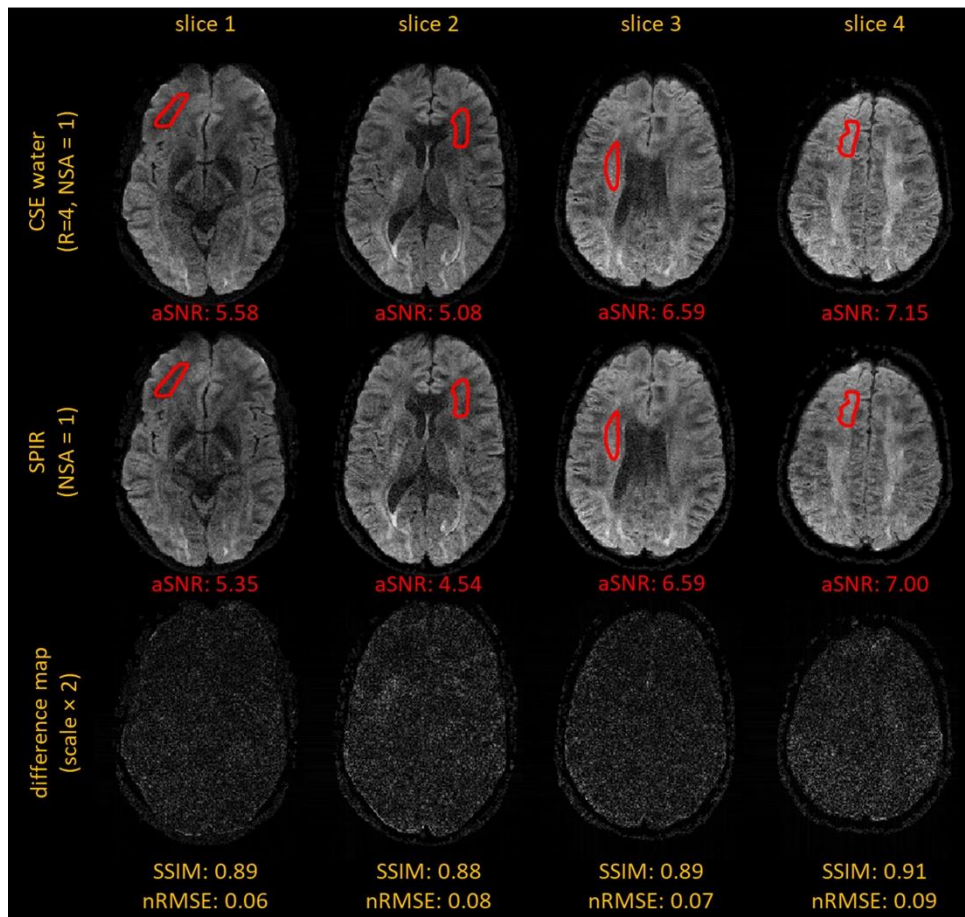


Figure 8. Comparison of low-rank-reconstructed water/fat resolved results to fat suppressed DWI data by means of SPIR. Water results for four retrospectively under-sampled brain DWI datasets ($b=1000$ s/mm²) using 4-point chemical shift encoding (Dixon)/4-shot data and fat suppression (SPIR) data with the same number of total shots. ROIs are selected in the frontal brain regions, focusing primarily on white matter, assuming minimal intensity variation within each ROI. The apparent SNR (aSNR) is given and shows good agreement between the two techniques, with a slightly lower aSNR for the SPIR images, possibly due to the use of additional measured navigators and potential MTC¹⁰⁰ from the fat suppression pulse. The difference maps show no discernible structural texture, indicating that no visible fat signal appeared in the water images that could have arisen due to a water-fat swap. Meanwhile, the overall high SSIM and low nRMSE values indicate comparable image quality in cases where fat suppression works well. The R=4 subsampling scheme is used corresponds to the one used in Fig 7(A).

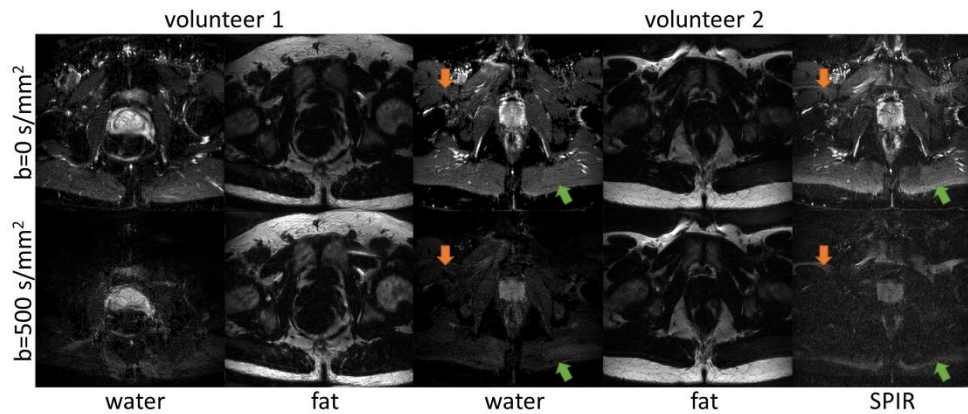


Figure 9. Two representative examples on application of our approach for prostate imaging (two different subjects). For volunteer 2 additionally acquired SPIR-data is also presented. Due to large B_0/B_1^+ inhomogeneities, failure of fat suppression can be seen in the SPIR images, whereas the proposed method does successfully remove such remaining fat signals in the water channel (marked by orange arrows). In addition, the fat signals from the olefinic peak (0.61 ppm relative to the water line), which are not suppressed by SPIR, are successfully separated by the proposed algorithm (green arrows).

6.5 Discussion

In this work, we demonstrated the effectiveness of using structured low-rank regularization for navigator-free water/fat separation in DW ms-EPI. This algorithm achieved consistent water/fat separated DW image quality in all the acquired data across different volunteers, slices, b-values. Fat suppression is always demanding in DWI when using EPI due to the low diffusivity and the large chemical-shift displacement of fat signals. Moreover, conventional fat saturation can be challenging due to the multi-peak spectrum fat model^{14,41,78,115}, which is difficult to be fully suppressed, via pre-saturation. In addition, fat suppression in B_1^+/B_0 inhomogeneous regions^{41,74,76,115,130} is prone to failure and may further degrade the SNR of the water signals due to magnetization transfer effects¹⁰⁰. Dixon methods, as an alternative, have been shown to be effective for DWI applications, as well as a smart choice for signal averaging, but the quality can be degraded due to shot-to-shot motion-induced phase variations. The proposed structured low-rank regularization method offers a solution by simultaneously separating water and fat signals and correcting shot-to-shot phase variations, without the use of navigators. Furthermore, we have shown that our approach allows for k-space under-sampling while still covering the full multi-shot/Dixon space extent. This allows Dixon-based water/fat separation in DW-ms-EPI without incurring any additional scan time penalty. Therefore, it can be a good alternative to conventional fat-suppressed DW-ms-EPI as it allows improved water/fat separation "for free". Finally, building upon the VCS

concept^{50,52,119,124}, the partial Fourier reconstruction demonstrated improved image quality while largely minimizing, though not entirely avoiding, blurring. Partial-Fourier enables a reduction in TE and thus, associated T₂-induced signal loss and is therefore of high interest in DWI.

In addition, our results showed that the proposed navigator-free approach leads to superior image quality and shorter scan times compared to extra-navigation methods. The unsuppressed but displaced fat signals in the measured navigators may cause artifacts, especially in regions where water and fat-signals are overlapping¹¹⁵ (shown in S.3), because that might lead to phase cancelations. In contrast, our low-rank regularization method can indirectly estimate the accurate phase variations of each shot while correcting for the fat-displacement.

In contrast to the water-fat resolved method (MSND) that uses an explicit shot-to-shot phase estimation through a Gauss-Newton method, the proposed method performs well even without a dedicated initialization of the phase maps. This is beneficial as the initialization (SENSE-based water/fat separation in MSND) can be unstable, especially in low SNR regions. Additionally, the minimization of the nuclear norm in the proposed approach, enforces the low-rankness of the Hankel matrices and recovers the individual complex shot images. The ability to leverage the redundant information across shots will further improve image quality compared to MSND, which is especially evident in the simulated low SNR case (Figure 2), in low SNR in-vivo cases such as those in the head-neck region (Figure.5), and when employing under-sampling (Figure S.3). For more detailed comparisons between and discussions on explicit phase map estimation methods and low-rank-based solutions, we refer the reader to relevant published works^{49-52,119}. It is worth noting that these works all dealt with fat suppressed ms-EPI data and therefore did not include Dixon to achieve water/fat separation.

In this study, there are several limitations that should be noted. One of them is the potential variation in the fat spectrum which depends on TE due to the different T₂ decay of each fat peak⁵⁴ and J-coupling¹³¹ and other experimental settings. In this work, a fat-spectrum model calibrated with a spin-echo sequence around TE=70 ms was adopted, which may not perfectly fit the brain scans (TE>100 ms) presented in this work. Fine calibration^{59,132} of the fat-spectrum model may be valuable for future work. Another limitation is regarding the macroscopic motion, which was not addressed in the current state and could affect the

reconstruction results (e.g., rigid/non-rigid motion between different images/Dixon points). Investigations on implementing an additional motion estimator, as demonstrated in some early work for fat-suppressed ms-EPI reconstruction^{45,46}, or even using fat as a navigation signal¹³³ could both be potential avenues for future research. In addition, it is important to emphasize that this is an initial study for reconstructing Dixon-DW-ms-EPI data using low-rank constraint, and as such, the results of this work have only been validated on a limited number of healthy subjects and have not been tested on patients or other anatomies. It would be beneficial to evaluate the performance of the method in a larger and more diverse cohort, as well as under different experimental conditions (e.g., higher segmentation factors, higher b-values with more critical SNR), which may affect the success of the method and should be considered in future investigations. Additionally, the chosen scan parameters (Table 1) and reconstruction parameters (e.g., using the same λ_1 and λ_2 for water and fat) were selected for testing purposes only, and the optimal values may vary across different anatomies/b-values/coils, necessitating further study. In cases where SNR is problematic (e.g., as demonstrated in S.3 with under-sampling in the head-neck region), the integration of denoising algorithms^{103,134,135} or the application of deep learning^{105,120}, especially in an iterative fashion, may also be attractive topics for future research. Different under-sampling patterns in the multi-shot/Dixon space are conceivable. Among them, those are preferable that minimize the noise propagation^{136,137} as shown in Figure 7.

Different from conventional fat-suppressed DW ms-EPI, the proposed acquisition and reconstruction scheme needs to reconstruct water / fat separated images while also estimating the shot-to-shot phase variations. Therefore, the magnitude average in each iteration is rather important to take advantage of the Dixon condition and guides the algorithm to reconstruct only one pair of joint water/fat magnitude images, as shown in Figure 4. Moreover, as illustrated in the simulation (Figure 2), when the SNR is low, the k-space filters which are often used in the “explicit” phase estimation methods^{45,47,115} can be adjusted to avoid large noise propagation. Further investigations, such as combining low-rank constraints in image-space⁵⁰, using phase-cycling¹³⁸ with joint multi-DW-direction reconstruction or applying total-variation for further regularization^{48,71}, could be attempted to boost the performance even more^{49,120}. Additionally, DTI^{49,120} can be considered as a future application with its under-sampling capability as another source for acceleration.

6.6 Conclusion

In this work we propose a structured low-rank-based reconstruction method for chemical-shift encoded DW-ms-EPI to jointly separate water/fat components and correcting for physiological motion-induced shot-to-shot phase variations. This approach has been proven to support under and partial-Fourier sampling allowing to adopt chemical-shift encoding as a smart way of fat suppression by exploiting its signal averaging properties. This helps to make the Dixon-ms-DWI sequence more flexible, avoiding time-consuming fat suppression and/or extra-navigation, and sampling just the diffusion encoded multi-shot data.

Acknowledgement

This work is part of the HTSM research program, project number 17104, and is partly funded by the Netherlands Research Council (NWO). The python implementation of the Iteratively Reweighted Least-Squares (IRLS) method is based on Dr. Merry Mani's IRLS-MUSSELS open source-code, for which we are very grateful.

References

1. le Bihan D, Mangin JF, Poupon C, et al. Diffusion tensor imaging: Concepts and applications. *Journal of Magnetic Resonance Imaging*. 2001;13(4):534-546.
2. Connolly M, Srinivasan A. Diffusion-Weighted Imaging in Head and Neck Cancer: Technique, Limitations, and Applications. *Magn Reson Imaging Clin N Am*. 2018;26(1):121-133.
3. Burakiewicz J, Charles-Edwards GD, Goh V, Schaeffter T. Water-fat separation in diffusion-weighted EPI using an IDEAL approach with image navigator. *Magn Reson Med*. 2015;73(3):964-972.
4. Burakiewicz J, Hooijmans MT, Webb AG, Verschuuren JJGM, Nix EH, Kan HE. Improved olefinic fat suppression in skeletal muscle DTI using a magnitude-based dixon method. *Magn Reson Med*. 2018;79(1):152-159.
5. Dong Y, Koolstra K, Riedel M, van Osch MJP, Börnert P. Regularized joint water-fat separation with B0 map estimation in image space for 2D-navigated interleaved EPI based diffusion MRI. *Magn Reson Med*. 2021;86(6):3034-3051.
6. Anzai Y, Lufkin RB, Jabour BA, Hanafee WN. Fat-suppression failure artifacts simulating pathology on frequency-selective fat-suppression MR images of the head and neck. *AJNR Am J Neuroradiol*. 1992;13(3):879.
7. Wendl CM, Eiglsperger J, Dendl LM, et al. Fat suppression in magnetic resonance imaging of the head and neck region: Is the two-point DIXON technique superior to spectral fat suppression? *British Journal of Radiology*. 2018;91(1085).
8. Dong Y, Riedel M, Koolstra K, van Osch MJP, Börnert P. Water/fat separation for self-navigated diffusion-weighted multishot echo-planar imaging. *NMR Biomed*. 2023;36(1):e4822.
9. Ren J, Sherry AD, Malloy CR. 1H MRS of intramyocellular lipids in soleus muscle at 7 T: Spectral simplification by using long echo times without water suppression. *Magn Reson Med*. 2010;64(3):662-671.
10. Hamilton G, Yokoo T, Bydder M, et al. In vivo characterization of the liver fat 1H MR spectrum. *NMR Biomed*. 2011;24(7):784-790.
11. Hernando D, Karampinos DC, King KF, et al. Removal of olefinic fat chemical shift artifact in diffusion MRI. *Magn Reson Med*. 2011;65(3):692-701.
12. Hu Z, Wang Y, Dong Z, Guo H. Water/fat separation for distortion-free EPI with point spread function encoding. *Magn Reson Med*. 2019;82(1):251-262.
13. Hernando D, Karampinos DC, King KF, et al. Removal of olefinic fat chemical shift artifact in diffusion MRI. *Magn Reson Med*. 2011;65(3):692-701.

14. Jeong HK, Gore JC, Anderson AW. High-resolution human diffusion tensor imaging using 2-D navigated multishot SENSE EPI at 7 T. *Magn Reson Med.* 2013;69(3):793-802.
15. Butts K, de Crespigny A, Pauly JM, Moseley M. Diffusion-weighted interleaved echo-planar imaging with a pair of orthogonal navigator echoes. *Magn Reson Med.* 1996;35(5):763-770.
16. Bammer R, Stollberger R, Augustin M, et al. Diffusion-weighted imaging with navigated interleaved echo-planar imaging and a conventional gradient system. *Radiology.* 1999;211(3):799-806.
17. An H, Ma X, Pan Z, Guo H, Lee EYP. Qualitative and quantitative comparison of image quality between single-shot echo-planar and interleaved multi-shot echo-planar diffusion-weighted imaging in female pelvis. *Eur Radiol.* 2020;30(4):1876-1884.
18. Jeong HK, Gore JC, Anderson AW. High-resolution human diffusion tensor imaging using 2-D navigated multishot SENSE EPI at 7 T. *Magn Reson Med.* 2013;69(3):793-802.
19. Guo H, Ma X, Zhang Z, Zhang B, Yuan C, Huang F. POCS-enhanced inherent correction of motion-induced phase errors (POCS-ICE) for high-resolution multishot diffusion MRI. *Magn Reson Med.* 2016;75(1):169-180.
20. Chen N kuei, Guidon A, Chang HC, Song AW. A robust multi-shot scan strategy for high-resolution diffusion weighted MRI enabled by multiplexed sensitivity-encoding (MUSE). *Neuroimage.* 2013;72:41-47.
21. Mani M, Jacob M, Kelley D, Magnotta V. Multi-shot sensitivity-encoded diffusion data recovery using structured low-rank matrix completion (MUSSELS). *Magn Reson Med.* 2017;78(2):494-507.
22. Mani M, Aggarwal HK, Magnotta V, Jacob M. Improved MUSSELS reconstruction for high-resolution multi-shot diffusion weighted imaging. *Magn Reson Med.* 2020;83(6):2253-2263.
23. Hu Y, Wang X, Tian Q, et al. Multi-shot diffusion-weighted MRI reconstruction with magnitude-based spatial-angular locally low-rank regularization (SPA-LLR). *Magn Reson Med.* 2020;83(5):1596-1607.
24. Hu Y, Levine EG, Tian Q, et al. Motion-robust reconstruction of multishot diffusion-weighted images without phase estimation through locally low-rank regularization. *Magn Reson Med.* 2019;81(2):1181-1190.
25. Dai E, Mani M, McNab JA. Multi-band multi-shot diffusion MRI reconstruction with joint usage of structured low-rank constraints and explicit phase mapping. *Magn Reson Med.* 2023;89(1):95-111.
26. Bilgic B, Chatnuntawech I, Manhard MK, et al. Highly accelerated multishot echo planar imaging through synergistic machine learning and joint reconstruction. *Magn Reson Med.* 2019;82(4):1343-1358.

27. Hu Z, Ma X, Truong TK, Song AW, Guo H. Phase-updated regularized SENSE for navigator-free multishot diffusion imaging. *Magn Reson Med.* 2017;78(1):172-181.
28. Kim TH, Setsompop K, Haldar JP. LORAKS makes better SENSE: Phase-constrained partial fourier SENSE reconstruction without phase calibration. *Magn Reson Med.* 2017;77(3):1021-1035.
29. Haldar JP, Zhuo J. P-LORAKS: Low-rank modeling of local k-space neighborhoods with parallel imaging data. *Magn Reson Med.* 2016;75(4):1499-1514.
30. Shin PJ, Larson PEZ, Ohliger MA, et al. Calibrationless parallel imaging reconstruction based on structured low-rank matrix completion. *Magn Reson Med.* 2014;72(4):959-970.
31. Blaimer M, Gutberlet M, Kellman P, Breuer FA, Köstler H, Griswold MA. Virtual coil concept for improved parallel MRI employing conjugate symmetric signals. *Magn Reson Med.* 2009;61(1):93-102.
32. Ren J, Dimitrov I, Sherry AD, Malloy CR. Composition of adipose tissue and marrow fat in humans by 1H NMR at 7 Tesla. *J Lipid Res.* 2008;49(9):2055-2062.
33. Fornasier M, Rauhut H, Ward R. Low-rank matrix recovery via iteratively reweighted least squares minimization. *SIAM Journal on Optimization.* 2011;21(4):1614-1640.
34. Berglund J, Rydén H, Avventi E, Norbeck O, Sprenger T, Skare S. Fat/water separation in k-space with real-valued estimates and its combination with POCS. *Magn Reson Med.* 2020;83(2):653-661.
35. Zee CS, Segall HD, Terk MR, et al. SPIR MRI in spinal diseases. *J Comput Assist Tomogr.* 1992;16(3):356-360.
36. Truong TK, Guidon A. High-resolution multishot spiral diffusion tensor imaging with inherent correction of motion-induced phase errors. *Magn Reson Med.* 2014;71(2):790-796.
37. Steinhoff M, Nehrke K, Mertins A, Börnert P. Segmented diffusion imaging with iterative motion-corrected reconstruction (SEDIMENT) for brain echo-planar imaging. *NMR Biomed.* 2020;33(12):e4185.
38. Chu ML, Chang HC, Chung HW, Truong TK, Bashir MR, Chen NK. POCS-based reconstruction of multiplexed sensitivity encoded MRI (POCSMUSE): A general algorithm for reducing motion-related artifacts. *Magn Reson Med.* 2015;74(5):1336-1348.
39. Zhang Z, Huang F, Ma X, Xie S, Guo H. Self-feeding MUSE: A robust method for high resolution diffusion imaging using interleaved EPI. *Neuroimage.* 2015;105:552-560.
40. Uecker M, Lai P, Murphy MJ, et al. ESPIRiT - An eigenvalue approach to autocalibrating parallel MRI: Where SENSE meets GRAPPA. *Magn Reson Med.* 2014;71(3):990-1001.

41. Uecker M. Making SENSE of Chemical Shift: Separating Species in Single-Shot EPI using Multiple Coils. *ISMRM*. 2012;20:2490.
42. Shin PJ, Larson PEZ, Uecker M, et al. Chemical shift separation with controlled aliasing for hyperpolarized ¹³C metabolic imaging. *Magn Reson Med*. 2015;74(4):978-989.
43. Wang Z, Bovik AC, Rahim Sheikh H, Simoncelli EP. Image Quality Assessment: From Error Visibility to Structural Similarity. *IEEE TRANSACTIONS ON IMAGE PROCESSING*. 2004;13(4).
44. Hong JH, Lee HY, Kang YH, et al. Improvement of Fat Suppression and Artifact Reduction Using IDEAL Technique in Head and Neck MRI at 3T. *Investig Magn Reson Imaging*. 2016;20(1):44.
45. Henkelman RM, Stanisz GJ, Graham SJ. Magnetization transfer in MRI: a review. *NMR Biomed*. 2001;14(2):57-64.
46. Hardy PA, Henkelman RM, Bishop JE, Poon ECS, Plewes DB. Why fat is bright in rare and fast spin-echo imaging. *Journal of Magnetic Resonance Imaging*. 1992;2(5):533-540.
47. BOTTOMLEY PA. Spatial Localization in NMR Spectroscopy in Vivo. *Ann N Y Acad Sci*. 1987;508(1):333-348.
48. Frahm J, Merboldt KD, Hänicke W. Localized proton spectroscopy using stimulated echoes. *Journal of Magnetic Resonance (1969)*. 1987;72(3):502-508.
49. Guhaniyogi S, Chu ML, Chang HC, Song AW, Chen NK. Motion immune diffusion imaging using augmented MUSE for high-resolution multi-shot EPI. *Magn Reson Med*. 2016;75(2):639-652.
50. Skare S, Hartwig A, Mårtensson M, Avventi E, Engström M. Properties of a 2D fat navigator for prospective image domain correction of nodding motion in brain MRI. *Magn Reson Med*. 2015;73(3):1110-1119.
51. Veraart J, Novikov DS, Christiaens D, Ades-aron B, Sijbers J, Fieremans E. Denoising of diffusion MRI using random matrix theory. *Neuroimage*. 2016;142:394-406.
52. Tristán-Vega A, García-Pérez V, Aja-Fernández S, Westin CF. Efficient and robust nonlocal means denoising of MR data based on salient features matching. *Comput Methods Programs Biomed*. 2012;105(2):131-144.
53. Fadnavis S, Batson J, Garyfallidis E. Patch2Self: Denoising Diffusion MRI with Self-Supervised Learning. 2020;(NeurIPS):1-11.
54. Tian Q, Li Z, Fan Q, et al. SDnDTI: Self-supervised deep learning-based denoising for diffusion tensor MRI. *Neuroimage*. 2022;253.
55. Breuer FA, Blaimer M, Mueller MF, et al. Controlled aliasing in volumetric parallel imaging (2D CAIPIRINHA). *Magn Reson Med*. 2006;55(3):549-556.

56. Pineda AR, Reeder SB, Wen Z, Pelc NJ. Cramér-Rao bounds for three-point decomposition of water and fat. *Magn Reson Med.* 2005;54(3):625-635.
57. Ong F, Cheng JY, Lustig M. General phase regularized reconstruction using phase cycling. *Magn Reson Med.* 2018;80(1):112-125.